Accepted Manuscript (*Journal of Alloys and Compounds*): 10.1016/j.jallcom.2021.162142

EQCM Study of Intercalation Processes into Electrodeposited MnO_2 Electrode in Aqueous Zinc-Ion Battery Electrolyte

*A. O. Efremova, A. I. Volkov, E. G. Tolstopyatova, V. V. Kondratiev**

Department of Electrochemistry, Institute of Chemistry, Saint Petersburg State University

7/9 Universitetskaya nab., St. Petersburg, 199034, Russian Federation

v.kondratev@spbu.ru

Abstract

In this work manganese oxide films were obtained by electrodeposition and their electrochemical and mass transfer processes in aqueous zinc-ion battery electrolyte were studied by cyclic voltammetry and electrochemical quartz crystal microbalance (EQCM). Cyclic voltammograms and corresponding mass variation curves of manganese oxide during charge-discharge processes were examined simultaneously on Au-coated quartz crystal electrodes. The investigations were conducted in aqueous electrolytes of different composition (2 M $ZnSO_4$ and 2 M $ZnSO_4$ + 0.1 M $MnSO_4$). Monitoring of electrode mass variation during potential cycling provides direct evidence that redox processes in MnO_2 electrodes co-occur with intercalation of protons and zinc ions. Combined CV and EQCM studies reveal that electrodeposited films of MnO_2 are unstable in 2 M $ZnSO_4$ electrolyte. The repeated potential cycling in Zn-containing electrolytes leads to rapid deterioration of electrode capacity in the few initial cycles due to the Zn^{2+} insertion into subsurface structures of MnO_2 and blocking of electroactivity of MnO_2 film on Au substrate. On the other hand, reversible processes of intercalation of protons and zinc ions occur in 2 M $ZnSO_4$ + 0.1 M $MnSO_4$ electrolyte. Two main steps of mass increase during the discharging process, taking place at 1.4 V (vs. Zn/Zn^{2+}) and in the potential range (1.3–1.0) V were demonstrated by EQCM. The first step of mass increase is mainly related to the intercalation of H^+ (as H_3O^+), whereas the second step of mass increase is mainly associated with formation of surface compounds like zinc sulfate hydroxide salts.

Keywords: manganese oxide; electrochemical deposition, mass transfer, EQCM, aqueous zinc ion battery;

1. Introduction

Lithium-ion batteries are the most effective power sources in our life. However, the increasing demands in large-scale application of lithium-ion batteries, especially for growing area of vehicles and power grids, are limited by lithium natural resources and relatively high cost of lithium [1,2]. Therefore, modern research trends focus on the development of novel multivalent-

ion batteries, of which aqueous zinc-ion batteries (AZIBs) are especially interesting. Despite more limited energy density and capacitive properties due to narrow electrochemical window of water-based electrolytes, aqueous zinc-ion batteries are interesting alternative power sources due to their low cost, nontoxicity, and relative abundance of the required materials [3–8].

The application of Zn anodes allows to reach high capacity (theoretical value 820 mAh g^{-1}) due to reversible processes in Zn/Zn^{2+} system possessing low oxidation potential (-0.762 V vs. SHE) [6]. Among electrode materials proposed as cathode materials for AZIBs, manganese oxides-based materials of different structures (including α-MnO_2[9–14], β-MnO_2 [15,16], γ-MnO_2 [17,18], and δ-MnO_2 [14,19–22]), and morphologies obtained using various synthesis approaches were objects of intense investigations in the latest decades. MnO_2 is an attractive material due to its high specific capacity (308 mA h g^{-1} based on a one-electron redox process Mn^{4+}/Mn^{3+}) and moderate discharge potential (+1.35 V), appropriate for practical purposes [5,23–26].

However, structural instability of electrode materials based on manganese oxides and the gradual dissolution of Mn^{2+} ions in aqueous electrolytes still remain unresolved issues, resulting in capacity fading and are the main challenges of these cathodes. The structural transformation of manganese oxides of different crystallographic polymorphs originates from the diversity of chemical bonding of structural octahedral MnO_6 units linked via edges and/or corners, giving different tunnel-type, layered-type, and spinel-type structures. Previous research has established that all these initially synthesized polymorphs gradually transform during charge-discharge cycling into forms that are more favorable for Zn intercalation, mostly into a Zn-buserite phase with large interlayer spacing, or spinel $ZnMn_2O_4$ phase as reported in [11,12,18,22,27,28]. Such observations were made from the first CV cycle with corresponding transformations of its shape, and it is also evident from detailed characterization of phases by *in situ* and *ex situ* XRD, XPS and other methods.

Based on the claims that one of the main reasons of capacity fading is the dissolution of Mn^{2+} ions from cathode, the additive of manganese(II) salts in the aqueous electrolyte was proposed [13]. Such additives turned out to be highly effective in improving the cycle performance of Mn-based cathodes and the use of Mn^{2+} additive in electrolytes has become a widespread approach in investigations of electrochemical performance of Zn/MnO_2 batteries [19–21,28–32].

More detailed investigations did not confirm the common opinion that Mn^{2+} additive in the aqueous Zn battery electrolyte could suppress manganese dissolution from MnO_2 cathode. It was suggested that the positive role of additive is more complex and includes the formation of a new phase of MnO_x from Mn^{2+} upon electrooxidation during charge cycles [20,28–30].

Regardless of the difference in the interpretation of the function and mechanism of the influence of the Mn^{2+} additive, it indeed improves the reversibility of Zn ion intercalation, leading

to more effective electrochemical performance of Zn/MnO_2 systems, as it was reported in recent papers [20,21,30,33].

However, despite abundance of published papers on electrode materials for AZIBs and many efforts achieved in understanding of charge storage by different approaches, the detailed mechanism of charge storage in Zn-containing electrolytes is still debated. Different concepts were proposed as possible mechanisms [4,5,13,21,29].

Two main issues related to electrochemical performance of Zn/MnO_2 systems are still debated: a) concurrent intercalation of Zn^{2+} and H^+ ions into the host electrode, and b) the mechanism of electrode reactions with conversion of synthesized or deposited MnO_2 structures into compounds that are more effective for reversible Zn^{2+} intercalation [3,6,28,29].

The participation of different cations (H^+/Zn^{2+} insertion) and formation of new phases are widely confirmed by *in situ* and *ex situ* XRD, XPS and other structure-sensitive methods. Moreover, along with these intercalation reactions of H^+ and Zn^{2+} insertion into manganese oxide, the redox process is also accompanied by formation of zinc sulfate hydroxide hydrate phase $Zn_4(OH)_6SO_4 \cdot xH_2O$ (ZHS) as a solid byproduct precipitate on electrode surface due to local pH variation [29,34–37]. An earlier study [37] also reported $Mn(OH)_2$ formation below 1.2 V, followed by formation of soluble Mn^{2+}, though later papers investigating systems with mild electrolytes have not presented such notion.

Along with these powerful structural methods, the EQCM method of investigation of mass transfer processes could also be useful for insertion-type electrodes. This *in situ* technique can provide precise data on mass change during electrode processes.

EQCM study of MnO_2 electrochemical deposition on Au electrodes and electrode processes were earlier investigated in several works [17,38–41]. The electrochemical behavior of manganese oxide electrodeposited at 1.0 V (SCE) on the gold-sputtered quartz electrode and the corresponding mass variation were investigated in neutral electrolytes containing 10 mM Na_2SO_4 both with and without $NaHCO_3$ or Na_2HPO_4 in [38]. For instance, the formation of a passive salt film on the manganese oxide surface has been reported, which hinders the dissolution of manganese oxides [38].

The results of EQCM investigations in electrolytes containing Mn^{2+} salts and multivalent cations (Na^+, Mg^{2+}, La^{3+}) are reported in [39]. The magnitude of mass variation was found to be approximately proportional to atomic weight of cations and dissolution of MnO_2 was relatively negligible. However, these investigations were conducted at relatively high scan rates (5–25 mV s^{-1}) and aimed at the characterization of MnO_2 as a pseudocapacitive material, where the reversible adsorption/desorption of cations mainly takes place.

EQCM investigations mentioned above confirm that the overall electrode reaction of MnO_2 electrodeposition due to Mn^{2+} ions oxidation to MnO_2 from different electrolytes occurs according to the equation:

$$Mn^{2+} + 2H_2O \rightarrow MnO_2 + 4H^+ + 2e^- \quad (1)$$

The redox process of Mn^{4+}/Mn^{3+} in different electrolytes is also commonly described [38,39] by the equation (2):

$$MnO_2 + H^+ + e^- \rightleftarrows MnOOH \quad (2)$$

The EQCM study of electrode processes of composite electrode material for AZIBs based on MnO_2 pre-intercalated with alkali ions ($K_{0.27}MnO_2 \cdot 0.54H_2O$ and $Na_{0.55}MnO_2 \cdot 1.5H_2O$) with addition of carbon black and PTFE binder was recently reported [36]. Along with *operando* X-ray diffraction techniques, it allowed the authors to confirm that the charge storage process for the studied Zn/MnO_2 system is dominated by the (de)intercalation of H_3O^+ with further dissolution-precipitation of $Zn_4(OH)_6(SO_4) \cdot 5H_2O$ solid product on the electrode surface during cycling.

The aim of this work is the study of the electrochemical and mass transfer processes in electrochemically deposited MnO_2 electrodes as binder-free cathodes for Zn-ion batteries in Zn^{2+} – and Zn^{2+}/Mn^{2+}– containing electrolytes. To the best of our knowledge, the EQCM measurements of mass transfer processes have not been reported for MnO_2-electrodeposited electrodes in 2 M $ZnSO_4$ + 0.1 M $MnSO_4$ aqueous electrolyte widely used in aqueous Zn-ion battery electrodes. This approach to investigation of charge-storage mechanism in AZIBs provides direct evidence of mass transfer processes and evaluation of contribution of mass transfer into overall electrode process, as well as identifies the mass input of proton and Zn-ion intercalation, and conversion reactions. The findings should make an important contribution to understanding of electrochemical performance of Mn-based aqueous Zn-ion batteries.

2. Experimental

2.1. Reagents and materials

Manganese sulfate ($MnSO_4$), manganese acetate $Mn(CH_3COO)_2$ and zinc sulfate ($ZnSO_4$) of analytical grade were obtained from Neva Reactive Co., Russia. Aqueous solutions were prepared on deionized water of resistivity not less than 18 MΩ, obtained by means of Millipore Direct-Q UV (Millipore Corp., USA) water purification system. Zinc foil (99.99%) was from Shanghai Metal Corp., China.

2.2. Electrochemical and EQCM measurements

All electrochemical studies were conducted in three-electrode electrochemical cells at room temperature (20 ± 2 °C) using a PGSTAT302N potentiostat/galvanostat (Metrohm Autolab,

The Netherlands) with Nova 2.1.5 software. For EQCM experiments the potentiostat was interfaced with a QCM200 instrument (Stanford Research Systems, USA).

The working electrodes for EQCM measurements were standard AT-cut quartz crystals with gold-coated working area, 1 inch diameter (Stanford Research Systems, USA), with a 5 MHz resonance frequency and the sensitivity factor $C_f = 56.6$ Hz cm^2 μg^{-1}, further denoted as "Au-quartz crystals".

The behavior of MnO_2 deposits as acoustically rigid films, necessary for the accuracy of the Sauerbrey equation for the determination of mass changes, was monitored by recording parameter V_c (the conductance signal is related to the series resonance resistance of the quartz crystal via (3) [42]).

$$R_m = 10000 \cdot 10^{-V_c/5} - 75 \quad (3)$$

The data on the change of frequency as a function of potential were converted into mass changes vs. potential or vs. charge in accord with the Sauerbrey equation:

$$\Delta f = -C_f \cdot \Delta m, \quad (4)$$

where Δf is the frequency variation (Hz), $C_f = 56.6$ Hz cm^2 g^{-1} is the sensitivity factor of the crystal, Δm is the mass change (μg cm^{-2}).

Two types of EQCM experiments were conducted:

1) Cycling of a pristine Au-quartz crystal electrode in the solution that contained both $ZnSO_4$ and $MnSO_4$ with the study of electrodeposition of MnO_2 during this process.

2) Cycling of the preliminarily deposited (from $Mn(CH_3COO)_2$) MnO_2 on an Au-quartz crystal electrode in either the electrolyte containing both $ZnSO_4$ and $MnSO_4$, or containing only $ZnSO_4$.

Electrochemical deposition of MnO_2 was conducted using a Pt wire auxiliary electrode and Ag/AgCl reference electrode. The cyclic voltammetry experiments were conducted using Zn auxiliary and reference electrodes. All potentials are given versus Zn/Zn^{2+} reference electrode (-0.762 V vs. SHE).

2.3. Electrochemical synthesis

Manganese oxide was deposited onto Au-quartz electrodes in potentiostatic conditions ($E = 1.0$ V) from an 0.1 M $Mn(CH_3COO)_2$ aqueous solution (pH ≈ 4.5) according to the modified procedure described in [38].

The deposition time was varied within (30–100) s. The active electrode mass was determined by Faraday's law and by direct measurement using EQCM. After synthesis, the electrodes were washed with deionized water and dried in electric oven with stepwise increasing temperature from ambient to 200 °C for 5 hours.

2.4. Structure and surface characterization

The X-ray diffraction (XRD) patterns of MnO_2 films were acquired on a Bruker AXS D2 Phaser X-ray diffractometer (Bruker GmbH, Germany) with Cu Kα radiation ($\lambda(CuK\alpha_1)$=1.54059 Å, $\lambda(CuK\alpha_2)$ = 1.54443 Å) in the 10°<2θ<90°range. Phase identification was performed with a PDXL2 (Rigaku) software using ICDD PDF-2 Powder Diffraction File database.

The morphology of MnO_2 films was characterized by using scanning electron microscopy (SEM) at accelerating voltage of 20 kV (SUPRA 40VP, Carl Zeiss, Germany). EDX analysis was performed with an energy-dispersive X-ray spectrometer X-act (Oxford Instruments, UK).

3. Results and discussion

3.1. Electrodeposition of manganese oxide

Fig.1 shows the Δm-Q curve of the MnO_2 electrodeposition process on an Au-quartz electrode from the 0.1 M $Mn(CH_3COO)_2$ solution at 1.0 V. The mass change was calculated from the frequency shift according to Sauerbrey equation.

As seen from Fig. 1, the mass–time curve for the deposition process was linear, so the rate of MnO_2 deposition was constant, and the mass change of electrodeposited MnO_2 was almost proportional to charge of synthesis. This agrees with data reported in the literature [38] and indirectly confirms formation of acoustically rigid film at these conditions.

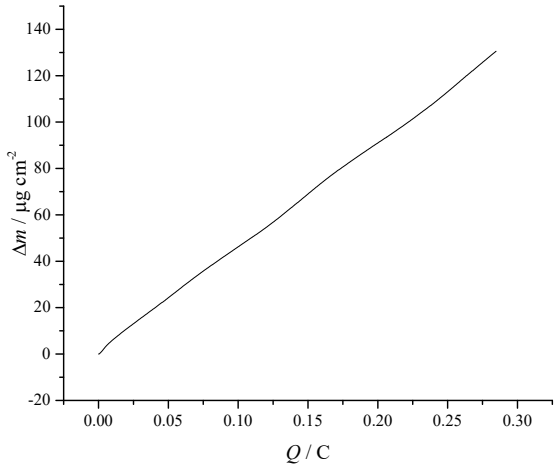

Fig.1. Mass change during deposition of MnO_2 on an Au-quartz crystal, E = 1.0 V; t = 100 s.

The electrodeposition of MnO_2 from mild acidic Mn^{2+}-containing solutions (pH 4.5) can proceed in accord with following overall oxidation reaction [38,39]:

$$Mn^{2+} + 2H_2O = MnO_2 + 4H^+ + 2e^- \quad (5)$$

The electrodeposited MnO_2 electrodes showed good reproducibility of CV shapes and consumed electrical charges at cycling.

3.2. Structural characterizations of electrodeposited MnO_2

The structure of the preliminarily electrodeposited MnO_2 films was identified by X-ray diffraction (XRD) analysis (Fig.2). As follows from the XRD pattern of electrodeposited MnO_2, the most intensive diffraction peaks can be well indexed to manganese oxide hydrate with formula $Mn_7O_{13}·5H_2O$ (ICDD card 00-023-1239) and orthorhombic crystal lattice.

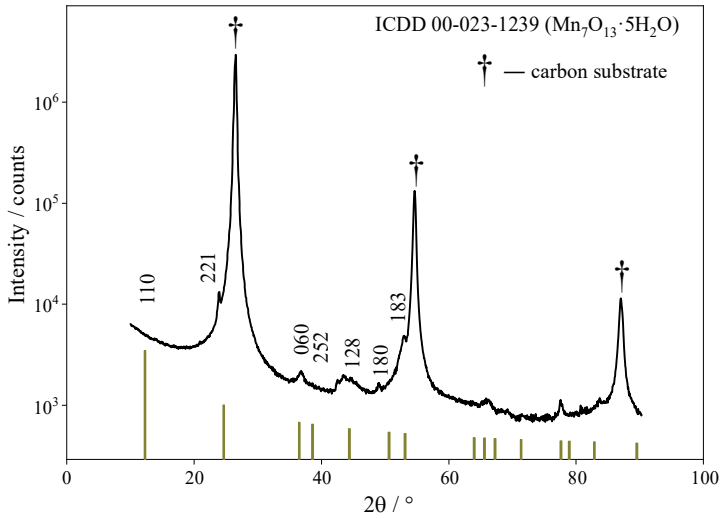

Fig. 2. XRD pattern of electrodeposited MnO_2. Deposition time: 200 s.

The initial surface morphology of MnO_2 thin films was investigated by scanning electron microscopy (Fig.3a,b,c). SEM images at low magnification show that MnO_2 films with grainy globular structure (Fig.3 a,b) uniformly cover the electrode surface, the average size of globular domains is about (1–2) μm. Images with higher magnification show that MnO_2 globules consist of randomly oriented nanowires with diameters about (10–20) nm and length (50–100) nm (Fig.3c). So, the nanowires form a three-dimensional network which can facilitate electrolyte penetration.

Similar SEM images of electrodeposited MnO_2 on an Au surface with nanowires forming a three-dimensional (3D) network have been previously reported [38,40].

As a consequence of porous nature of MnO_2 layer on the electrode surface, keeping the electrode in air and its gradual drying before *ex situ* SEM measurements caused some cracks of the film. The EDX analysis (Fig. S1, S2) of the films revealed the presence of oxygen and manganese in a 1.63 O to 1 Mn average atomic ratio (Table S1).

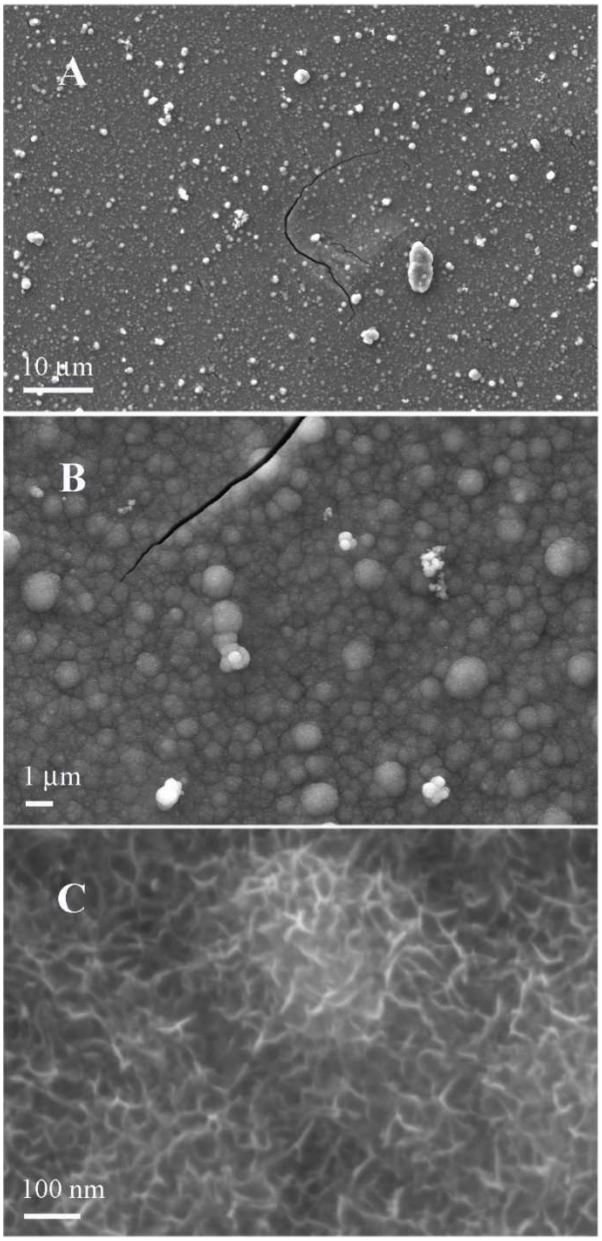

Fig.3. SEM images of MnO_2 films at different magnifications.

Cyclic voltammetry of MnO_2 electrodeposited on Au-quartz electrodes was performed in 1.0–1.8 V (vs. Zn/Zn^{2+}) potentials range in 2 M $ZnSO_4$ + 0.1 M $MnSO_4$ aqueous electrolyte (pH 4.5), widely used in Zn-ion batteries with manganese oxide-based cathodes [11–14,18,20,22]. The evolution of CVs recorded during electrodeposition of MnO_2 on the electrode during subsequent charge–discharge processes in the presence of Mn^{2+} ions in solution is shown in Fig.4.

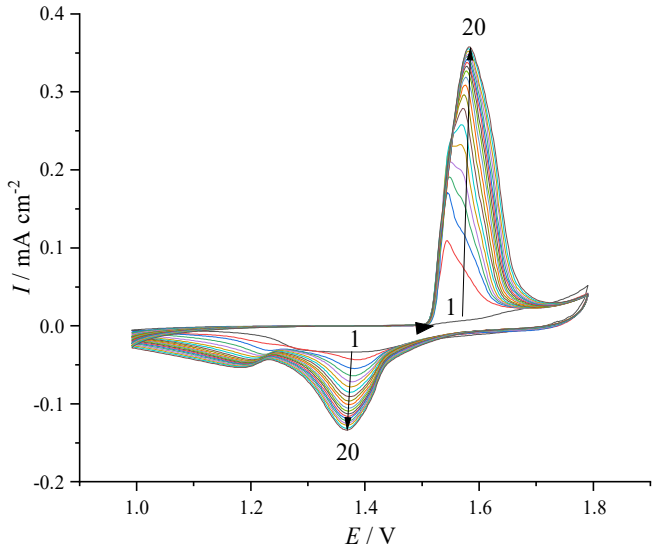

Fig.4. Evolution of CVs of Au/MnO_2 electrode during cycling in 2 M $ZnSO_4$ + 0.1 M $MnSO_4$ electrolyte. The first positive scan starts from E=1.5 V.

The anodic peak appearing at 1.6 V in the initial cycles corresponds to oxidation of Mn^{2+} to MnO_2 and deposition of newly formed layers onto the electrode surface. At the negative scan there are two initial reduction peaks, that in accord with literature data are usually associated with Mn^{3+}/Mn^{4+} redox process with consecutive intercalation of protons (at 1.38 V) and zinc ions, or/and ZHS precipitation (at 1.18 V) [13,29,34,35,40]. The anodic peak gradually transforms into two unresolved peaks and both of them shift to more positive potentials in subsequent cycles. These two poorly resolved peaks (at potentials approx. 1.5 V and 1.6 V) correspond to extraction of counter-ions and oxidation of Mn^{3+} ions, respectively. Both cathodic and anodic peaks regularly increase with the number of cycles, indicating the progressive electrodeposition of MnO_2 with a slowdown in current growth per cycle. This is a typical electrochemical behavior of MnO_2-based electrodes, and these results are qualitatively well-consistent with the data available in the literature for many other structural types of MnO_2, according to which MnO_2 structures are transformed during the first redox cycle.

During the charge process (positive scan) of electrodes with relatively thick MnO_2 films two main possible mass transfer processes may proceed: extraction of counter-ions from the MnO_2 crystal lattice and deposition of new layers of MnO_2 on electrode. Both these processes occur at almost the same potential. The extraction of counter ions (at 1.55 V) precedes deposition of new phase layer of MnO_2 (at 1.62 V).

The frequency and corresponding mass variation during potential cycling of Au/MnO_2 electrode in Mn^{2+}-containing electrolyte are shown in Fig.5 for five initial cycles for more convenient data presentation. We can see gradual decrease of frequency of an Au-quartz crystal

electrode oscillations with the number of cycles which clearly indicates the general increase of electrode mass cycle by cycle, which is attributed to the formation of electrodeposited MnO_2 layers (Fig.5a). The typical patterns of mass variations were well reproducible in parallel experiments suggesting the reversible intercalation/deintercalation processes.

The Δm–E profiles calculated from initial raw Δf–E data using Sauerbrey equation are displayed in Fig.5b. The magnitude of the sharpest mass steps at 1.55 V in the positive scan and at 1.2 V in the negative scan increased with the number of cycles, i.e., with the increase of total mass of MnO_2 deposit.

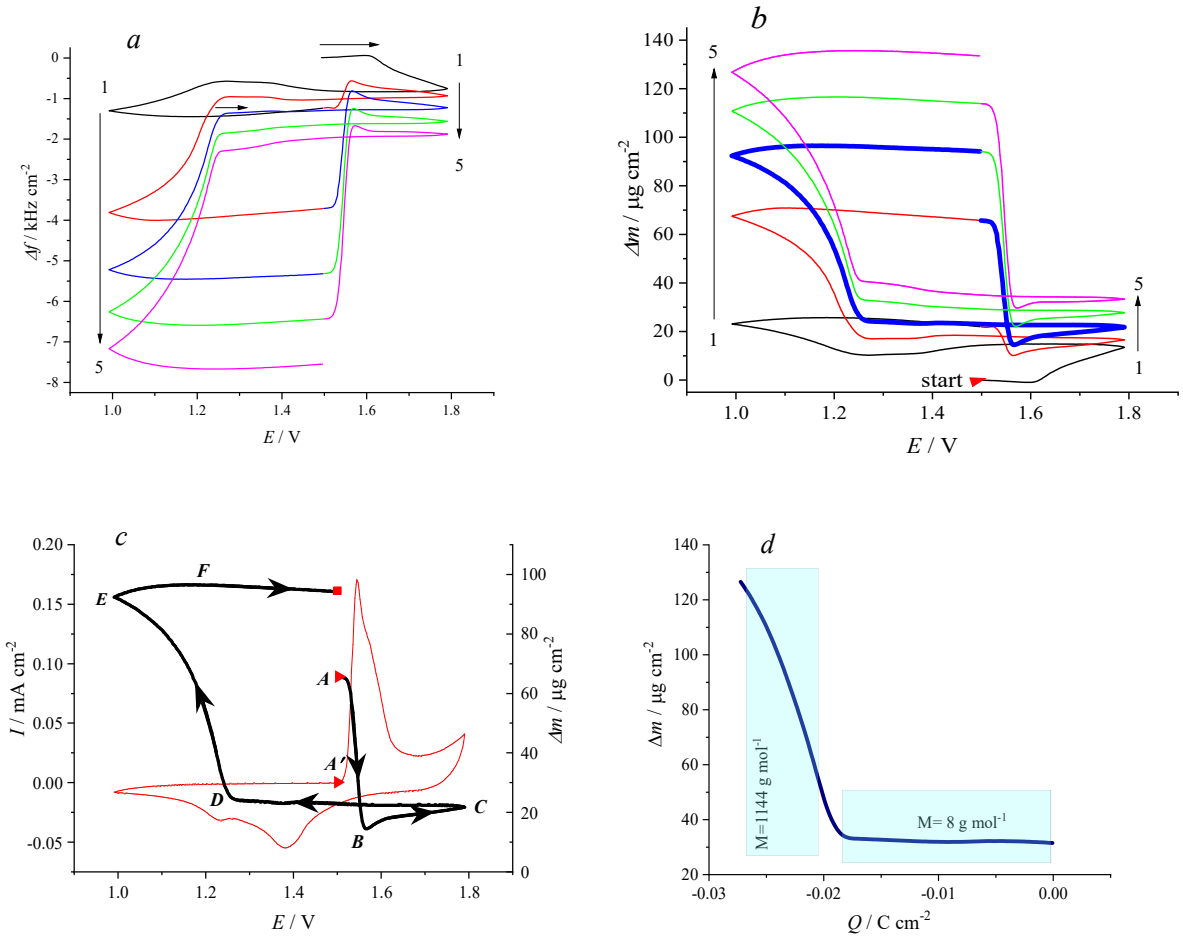

Fig.5. *EQCM studies of Au/MnO_2 electrode during potential cycling in 2 M $ZnSO_4$ + 0.1 M $MnSO_4$ electrolyte: a – frequency variation vs. potential, b – mass variation vs. potential, c – selected CV and Δm-E cycle (the 3rd cycles), d – the mass-charge dependence of Au/MnO_2 electrode for the negative scan in 2 M $ZnSO_4$ + 0.1 M $MnSO_4$ electrolyte (based on data of Fig. 5c).*

Fig.5c displays selected voltammetric cycle (3rd) and corresponding mass variation vs. potential for more close visual inspection of the shape of Δm–E profile. The starting points ***A*** and ***A'*** for mass change cycle and CV cycle, respectively, are marked on the curves, and the directions of potential scan and the mass variation vs. potential are shown on the curves by arrows.

Starting from the point ***A*** moving to the point ***B*** we see the sharp decrease of the electrode mass due to extraction of protons and dissolution of zinc precipitates, which formed during the

previous negative scan, from the MnO_2 electrode. This process of extraction of protons and dissolution of zinc precipitates (at 1.55 V) agrees with the sharp first CV peak of oxidation. It is followed by a small increase of electrode mass at the ***B-C*** segment (1.58–1.8 V), which may originate not only from dominant process of electrodeposition of manganese oxide but also from the ongoing ***A-B*** process related to extraction of counter-ions.

When the scan is reversed to the negative direction, in the potential range (1.8–1.25) V, a slight mass gain is observed (***C-D*** segment) due to H^+ insertion, followed by a sharp mass gain in the ***D-E*** segment of the curve (1.25 V to 1.01 V) probably due to the process of intercalation of Zn^{2+} ions and/or precipitation of insoluble byproducts like ZHS on manganese oxide particles and in the porous space between the grains. The latter process is more favorable due to further gradual increase of the pH value of the electrolyte in the vicinity of the electrode surface, which is associated with H^+ insertion process and the disproportion of unstable Mn^{3+} ions formed during partial dissolution of manganese oxide as reported in [34,36]. This conclusion will be supported by further analysis of mass – charge dependence in Fig.5d. The formation of ZHS surface compound may act as a kind of SEI layer counteracting the phase transition of initial MnO_2 into Zn-containing phase. As it was reported earlier [20], such phase transformation of MnO_2 into Zn-containing phases (like $Zn_xMn_2O_4$) is considered as the main cause of capacity fading.

When the scan is reversed to the positive direction (***E-F*** segment), a slight mass gain still occurs in the (1.0–1.2) V potential range due to ongoing chemical precipitation of ZHS. Thus, the reversible processes of mass changes taking place in MnO_2 films are related to mass increase due to H^+ insertion and formation of surface compounds like zinc sulfate hydroxide salts on the negative scan, whereas on the positive scan the decrease of mass takes place due to ions de-intercalation together with dissolution of ZHS at pH decrease near the electrode surface.

In addition, it should be noted that a small mass step (increase) takes place at potentials around 1.4 V at the H^+ insertion, which is more visible in the last cycle, where the magnitude of mass change is higher (see Fig. 5b, cycle 5).

The mass–charge dependence for Au/MnO_2 electrode was calculated for the selected 3rd cycle of Fig.5c. Figure 5d shows two characteristic regions of the electrode mass change vs. the charge during the negative scan: ***I*** – a gently sloping region with average apparent molar mass of moving species M_{app}=8 g mol^{-1}, which most likely corresponds to the intercalation of protons, and ***II*** – a short steep mass change, corresponding to the average value of apparent molar mass of transferred particles M_{app}=1144 g mol^{-1}. This mass change is much higher than the molar mass of zinc ions expected in the case of conventional Zn^{2+} intercalation and it could be mainly associated with the chemical deposition of ZHS due to pH increase.

Fig. 6a,b shows the first 3 cycles of CV and *Δf–E* curves of Au/MnO_2 electrode for pure $ZnSO_4$ electrolyte. MnO_2 electrode shows two peaks (at 1.38 V and 1.5 V) only in the first negative scan. The dramatic fading of capacity proceeds in the following cycles, and all anodic and cathodic peaks almost disappear (Fig. 6a). This result clearly demonstrates that zinc ions cannot be reversibly inserted into crystal lattice of preliminarily prepared MnO_2 layer. The corresponding Δ*f–E* curves (Fig. 6b) in the first scan display a small step of frequency change at 1.4 V which probably corresponds to intercalation of protons with minor change of mass and a huge drop of frequency (increase of mass) at potentials below 1.2 V, related to the dominating process of ZHS precipitation. The analysis of the mass–charge dependence for the first negative cycle is shown in Fig. S3. In the following 2-3 cycles the frequency goes down slower, indicating continued increase of electrode mass in the (1.0–1.4) V range of potentials (Fig. 6b).

We can exclude the de-attachment of MnO_2 from substrate as a consequence of Zn^{2+} intercalation, because in this case the decrease of mass would be expected.

So, in pure $ZnSO_4$ electrolyte we have an opposite case of electrode behavior in comparison to the electrolyte with Mn^{2+} additives. We do not see reversible mass change observed in the case of mixed Mn^{2+}-Zn^{2+} containing electrolyte and the decrease of electrode mass at positive scan around 1.55–1.6 V, which was mainly related to the dissolution of ZHS precipitate. Instead of gradual conversion in mixed electrolyte, the fast decrease of electrode capacity and irreversible increase of electrode mass takes place in the electrolyte without Mn^{2+} additive.

However, based on the data obtained, we cannot specify the exact cause of such an irreversible change in mass. Two main causes could be assumed: i) the irreversible mass change takes place at the fast blocking of the electroactivity of initial MnO_2 film on the electrode by trapped/adsorbed Zn^{2+} ions into crystal lattice; ii) the irreversible precipitation of insulating ZHS takes place. The conclusion on the precipitation of ZHS is supported by estimated apparent molar mass of about 814 g mol^{-1} for first cycle in potential region below 1.3 V (see Fig.S3). The precipitation of ZHS will probably mask the possible contribution of Zn^{2+} intercalation in the overall mass change, therefore, it is hard to confirm the latter process.

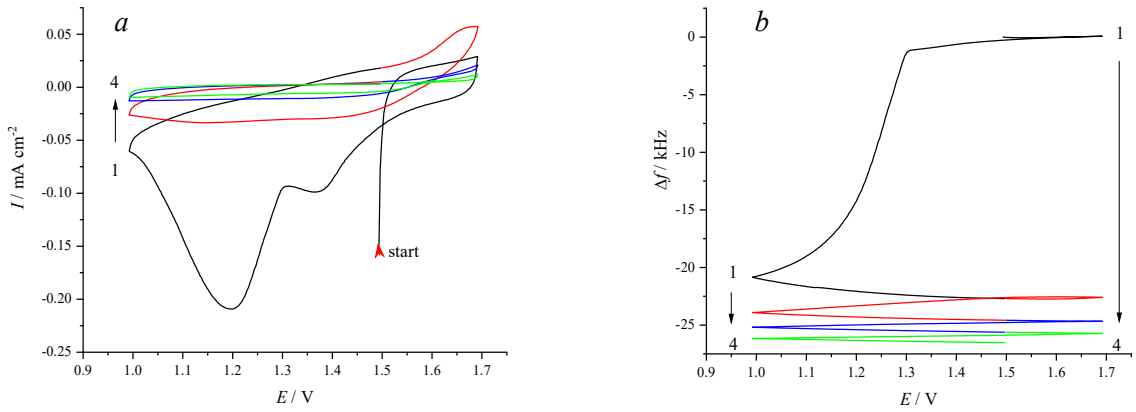

Fig.6. *a – cyclic voltammograms, b – frequency variation of Au/MnO_2 electrode during potential cycling in2 M $ZnSO_4$ electrolyte. The first positive scan starts from E=1.5 V.*

To understand further the processes proceeding at the electrodeposition of MnO_2 from Zn-ion battery aqueous electrolyte with Mn^{2+} additive, the CV measurements and simultaneous monitoring of mass changes by EQCM were conducted on a bare Au-quartz electrode without preliminary electrodeposited MnO_2. We have tested the case of electrode processes proceeding in battery electrolyte with Mn^{2+} additive, where newly formed MnO_2 structures are deposited on the surface of the electrode upon cycling, which in most cases were identified as ε-MnO_2 structures forming *in situ* on the electrode surface [20,28,30,33].

In this case, development of the shape of CVs with cycle number was similar. In Fig.7a, the first CV cycle shows typical electrochemical behavior of MnO_x with only one cathodic peak centered at 1.37 V and one anodic peak at 1.58 V. With prolonged cycling, the second cathodic peak appears at 1.07 V and the complex anodic peak shifts to more positive potentials. With an increase of the cycle number, the increase in current gradually slows down due to the increase of MnO_2 thickness and its resistance (Fig. 7a).

Fig.7b shows the dependence of the frequency shift of quartz electrode vs. potential, recorded simultaneously with cyclic voltammograms. The constant shift of frequency of an Au-quartz electrode with number of cycles clearly indicates the general increase of electrode mass cycle by cycle due to the formation of electrodeposited MnO_2 layers. The magnitude of most sharp mass steps at 1.55 V in the positive scan and at 1.2 V in the negative scan also increases with the number of cycles, i.e., with the increase of mass of MnO_2 deposit. In the beginning of cycling and during prolonged cycling, the patterns of mass variation vs. potential are different (Fig. 7c).

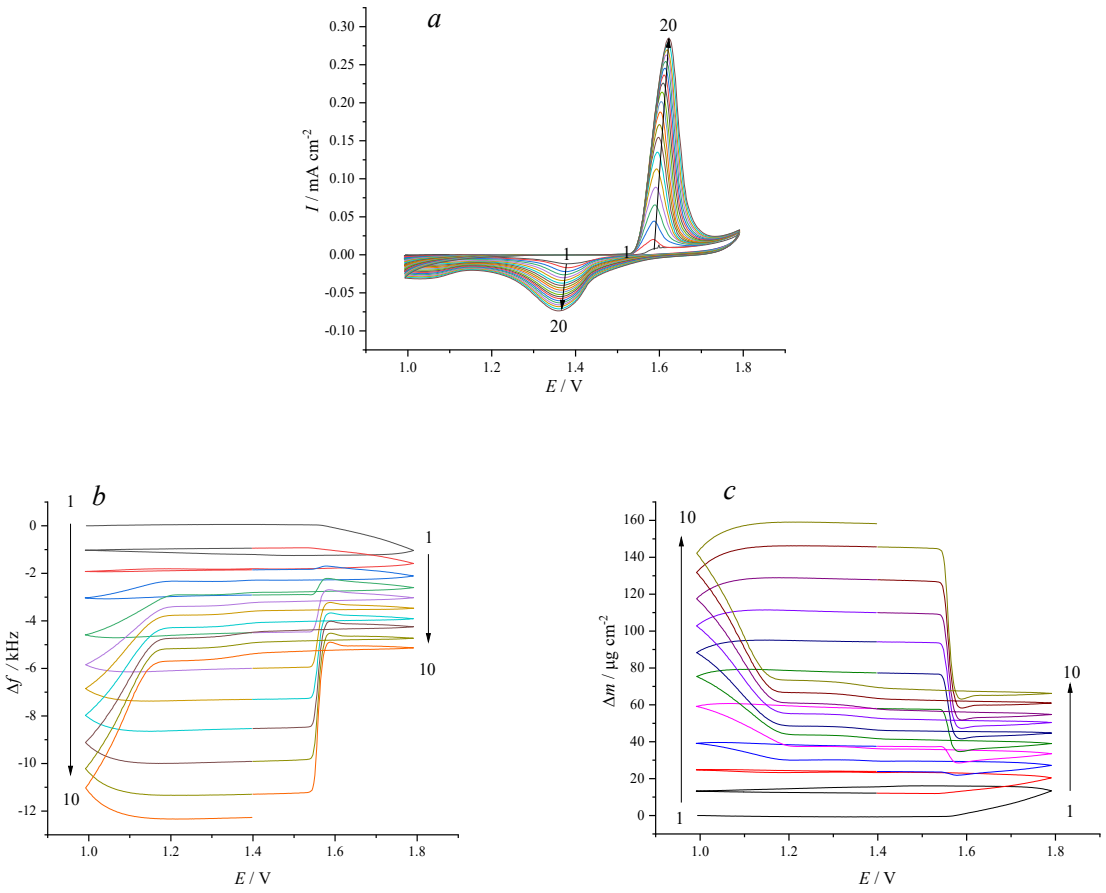

Fig.7. a – evolution of CVs of a pristine Au-quartz electrode, b – frequency variation and c – mass variation during cycling in 2 M $ZnSO_4$ + 0.1 M $MnSO_4$ electrolyte.

To follow the peculiarities of mass variation at the beginning of electrodeposition process and at prolonged cycling more precisely, in Fig.8a,b we present selected Δ*m*–*E* profiles, calculated from raw Δ*f*–*E* data. In contrast to the aforementioned case (Fig.5a), different Δ*f*–*E* profiles are observed for initial (2–5) and higher cycle numbers (10-15).

First, let us consider the case in Fig. 8a, where mass variation with potential is simple. If we start from the point ***A*** by positive scan to the point ***B*** (see e.g., cycle 5), we can see the increase of electrode mass at potentials above 1.6 V, resulting from the dominant process of electrodeposition of MnO_2 on the electrode surface. Although the scan reverses to negative direction, in the (1.8–1.7) V potential range the mass gain proceeds due to continued electrodeposition process. Then, as the back scan continues, below 1.5 V (segment ***C-D***) a gradual small decrease of mass takes place probably due to partial dissolution of MnO_2.

Obviously, for thicker MnO_2 films, with increase of number of cycles the mass loss from expelling of counter ions is getting more significant than the mass gain due to additional MnO_2 deposition (Fig.8b).

Fig.8c displays the representative *Δm*–*E* profile and simultaneous CV cycle for closer visual inspection of the shapes of *Δm*–*E* profiles for higher cycle numbers. As seen from the data

presented in Fig.8c, the typical shapes of *Δm–E* profile of a pristine Au-quartz electrode maintained during potential cycling are close to the ones of Au/MnO_2 electrodes, indicating similar mass transfer processes taking place in pre-deposited MnO_2 films and MnO_2 films formed from battery electrolyte.

For simplicity of discussion of the most interesting typical case of *Δm–E* profile (Fig.8c), we have also divided it into several characteristic regions for positive and negative CV branches. The points on the selected profile allow to follow the stepwise change of mass at different potentials. In the positive scan starting from the point ***A*** to the point ***B,*** we can see a sharp loss of mass in the narrow potential range of (1.55–1.58) V, which occurs due to predominant oxidation process with extraction of counter-ions and dissolution of ZHS precipitate from the electrode. Then, a gradual increase of electrode mass (segment ***B-C***) occurs at potentials higher than 1.6 V due to the newly electrodeposited layers of MnO_2 on the electrode surface from the Mn^{2+}-containing electrolyte.

On the negative scan, in the range between the points ***D*** and ***E,*** a mass step at 1.38 V takes place, which we ascribe to a low-mass charge carrier intercalation (H^+) at the Mn^{4+}/Mn^{3+} redox transition during cycling with the formation of MnOOH as the main solid product on the electrode. Then, at the transition from the point ***E*** to the point ***F***, a more significant step of mass increase related to precipitation of ZHS takes place. After the reverse of potential scan direction from 1.0 V to more positive values (segment ***F-G***) a well-pronounced step of mass increase is likely related to the ongoing chemical precipitation of ZHS on the electrode surface (up to 1.2 V). This pattern of mass change vs. potential (Fig.8c) is quite repetitive at the displayed cycles with increase of magnitude of mass/frequency changes from cycle to cycle caused by continuous increase of the deposit mass. The reproducibility of CVs and mass variation suggests reversible charge-discharge processes.

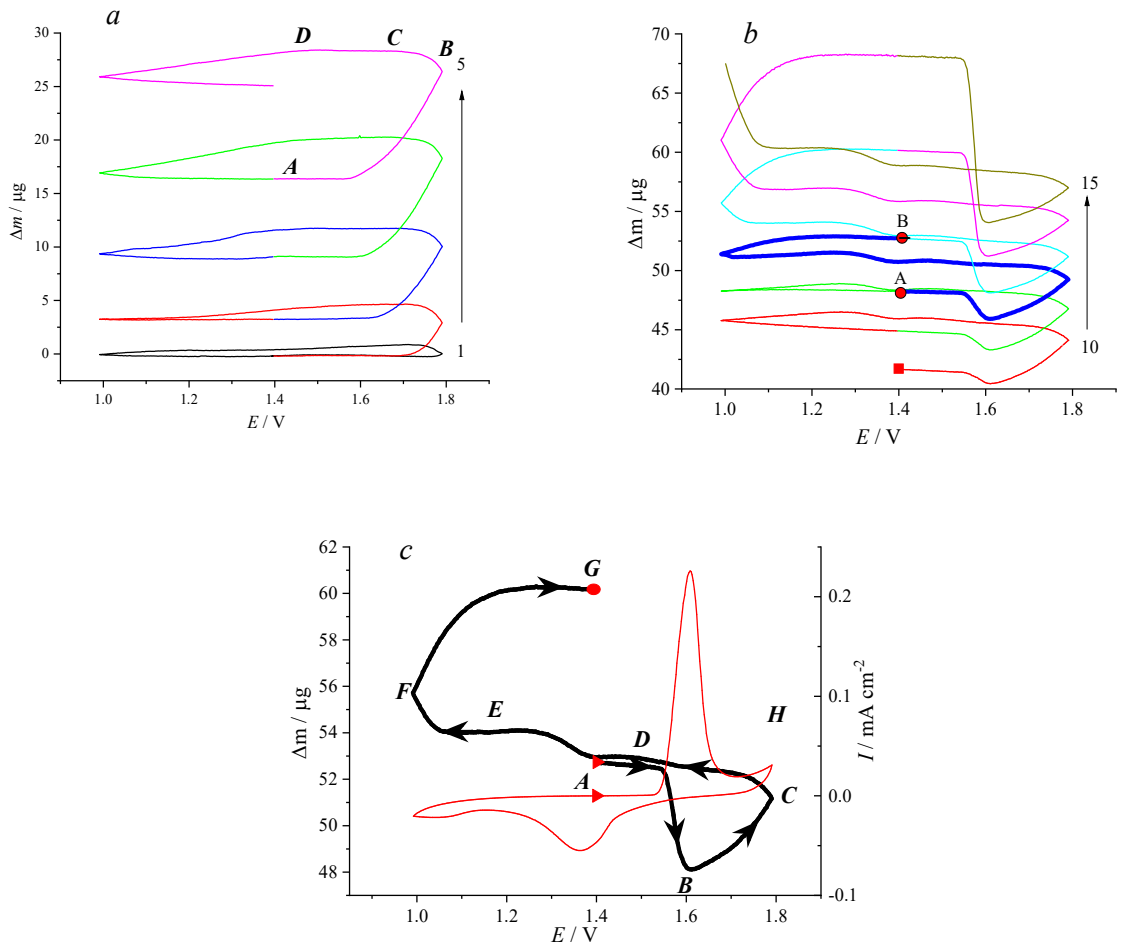

Fig.8. *Δm–E curves of uncoated Au-quartz electrode during potential cycling in 2 M $ZnSO_4$ + 0.1 M $MnSO_4$ electrolyte: a – five initial cycles, b – 10^{th} -15^{th} cycles, c – detailed view of the 13^{th} CV cycle.*

The mass–charge (Δ*m*–*Q*) curve (Fig. 9) was plotted based of data of Fig.7. Two easily distinguishable types of patterns of electrode mass changes with monotonic almost linear change of electrode mass with charge were observed for the regions ***I*** and ***II***. These data allow to estimate the apparent molecular mass of the transferred species at the electrode process in accord with

$$M_{app} = zF(d\Delta m/dQ), \quad (6)$$

where Q is the coulombic charge measured (mC), $d\Delta m$ is the electrode mass change (μg), F is the Faraday's constant (96485 C mol^{-1}) and z is the number of electrons exchanged in the redox reaction.

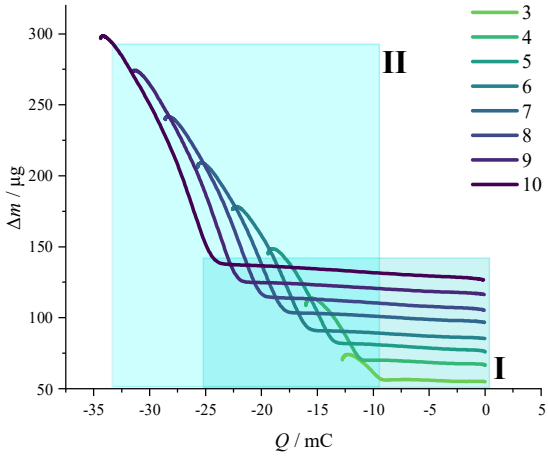

Fig.9. The mass – charge dependence of uncoated Au-quartz electrode for several negative scans in 2 M $ZnSO_4$ + 0.1 M $MnSO_4$ electrolyte (based on data of Fig. 7).

It should be noted here that in this case the values of apparent molar mass of transferred species might be only tentative due to complex nature of mass changes in the system and contribution from solvent molecules to the overall mass transport process. Therefore, the calculations of exact molar masses should be approached with caution. Nevertheless, analysis of Δm–Q plots for separate cycles (Fig. 9) was performed, which allowed to estimate the average apparent molar mass (M_{app}) of moving species. The analysis of Δm–Q plots reveals the drastic change of M_{app} values for different potential regions (Fig.9, regions ***I*** and ***II***). It was found that the values of M_{app} vary in the range of (11–29) g mol^{-1} for region ***I*** and in the range of (900–1600) g mol^{-1} for region ***II***, respectively.

This result suggests that the redox transition in the potential region (1.8–1.3) V mainly involves intercalation of H^+ (probably as H_3O^+ with co-intercalation of water molecules), which is in general agreement with the literature data. In the potential region (1.3–1.0) V formally calculated values of M_{app} were much higher, reaching values of (900–1600) g mol^{-1}. Similar values of M_{app} were obtained from analysis of data of Fig. 5 in the case of preliminary electrodeposited MnO_2 film on the electrode. The obtained values are much higher than the molar mass of zinc ions, which could be assumed to be the possible moving species in the case of conventional intercalation process. This result can be interpreted by considering an additional chemical precipitation of surface compounds like zinc sulfate hydroxide $Zn_4(OH)_6SO_4{\cdot}xH_2O$ during discharge process at potentials lower than 1.2 V which were recently proposed as byproducts [13,24,30,36,43]. It is reasonable to assume the formation and dissolution of surface compounds such as ZHS, because the appearance of such products in the potential region (1.0–1.3) V was reliably confirmed earlier by different *in situ* structural methods [24,30].

It is also worth noting that the precipitation/dissolution process of $Zn_4(OH)_6SO_4 \cdot xH_2O$ taking place during consecutive cycles is reversible, as was directly confirmed by mass monitoring in our study of electrodeposited MnO_2. These data are in good agreement with EQCM results, obtained earlier by EQCM study for composite electrode based on MnO_2 pre-intercalated with alkali ions ($K_{0,27}MnO_2 \cdot 0.54\ H_2O$ and $Na_{0,55}MnO_2 \cdot 1.5\ H_2O$) with addition of carbon black and PTFE binder [36]. During the charging process the electrode mass is partly recovered by sharp decrease at 1.6 V, which indicates that these surface deposits are leaving the electrode at the positive scan due to the local pH changes at electrode/electrolyte interface as reported in [13,24,30,34,36,43].

The results of this work support the conclusions made in some recently published papers [13,20,34,36,43], that instead of commonly considered conventional Zn^{2+} intercalation processes, the reversible process with H^+ insertion and accompanying formation of zinc sulfate hydroxide on the surface and in porous spaces of electrode takes place.

Based on the patterns of behavior of such redox systems, it is likely that the electrochemical and mass transfer behavior of the Zn/MnO_2 system will be also significantly dependent on the thickness of electrodes (amount of MnO_2), electrolyte pH values and their buffer properties.

As follows from the discussion of results, in general, Δm–E dependencies, obtained for the two types of EQCM experiments (i.e., for preliminarily deposited MnO_2 films and for bare electrodes with MnO_2 formed during potential cycling in Mn^{2+} containing electrolyte), are qualitatively similar. However, they also have some significant peculiarities, which may be associated with different amount of MnO_2 on the electrode surface.

Approaching the critical pH values near electrode surface, necessary for deposition of ZHS, is probably dependent on the total amount of MnO_2 on the electrode surface and it could be kinetically limited by H^+ insertion for thicker film of manganese oxide.

An additional argument in favor of the importance of total amount of MnO_2 deposit are the peculiarities of Δm–E dependencies for preliminarily deposited MnO_2 films and for electrodes with MnO_2 formed during potential cycling. In the case of deposition of small amount of MnO_2 during the 1st and the 2nd initial cycles (Fig. 8a), noticeable mass increase related to ZHS deposition is not observed, probably due to insufficient increase of local pH coming from intercalation of small amount of H^+ ions into MnO_2. Further systematic research of these peculiarities is needed to make more detailed conclusions on the mechanism of charge storage in the Zn/MnO_2 system.

Conclusion

In this study, MnO_2 films were electrodeposited on an Au-quartz crystal electrode and their electrochemical properties were studied in 2 M $ZnSO_4$ electrolyte and mixed 2 M $ZnSO_4$ +0.1 M $MnSO_4$ electrolyte. Combined CV and EQCM analysis revealed that the repeated potential cycling

of MnO_2 in $ZnSO_4$ leads to rapid deterioration of the electrode capacity in the few initial cycles due to the Zn^{2+} insertion into subsurface structures and blocking of electroactivity of MnO_2 film on an Au substrate. Reversible processes of mass changes due to intercalation of protons and formation/dissolution of $Zn_4(OH)_6SO_4 \cdot xH_2O$ surface compounds were observed in 2 M $ZnSO_4$ + 0.1 M $MnSO_4$. Two steps of mass increase during the discharging process are assigned to the intercalation of H^+ (1.4 V) and the precipitation of Zn^{2+}-containing insoluble byproduct. The magnitude of apparent molar mass of species transferred in the range of potentials around the first cathodic peak (at 1.4 V) is approximately proportional to the molecular mass of H_3O^+ ions. This peak at 1.4 V dominates since the contribution to capacity and therefore the storage mechanism is mainly determined by proton intercalation. The analysis of the mass step at negative scan in the range of potentials (1.3–1.0) V gives the value of apparent molar mass much higher than that of Zn^{2+} ions, supporting the hypothesis of additional $Zn_4(OH)_6SO_4 \cdot xH_2O$ precipitation/dissolution reactions recently proposed in the literature. It is a consequence of gradual increase of the pH value of the electrolyte in the vicinity of electrode surface at discharge, which is associated with H^+ insertion process and the disproportion of unstable Mn^{3+} ions formed during the partial dissolution from manganese oxide, as reported in [43]. During the charging process, the electrode loses part of its mass, as seen from the sharp mass decrease at 1.6 V, indicating that ZHS surface deposits dissolve and leave the electrode at the positive scan due to the local pH changes at electrode/electrolyte interface.

These results show that the presented approach with *in situ* EQCM measurements is highly useful for further understanding of the intercalation processes in metal oxide cathodes of zinc-ion systems.

Acknowledgements

The financial support from Russian Foundation for Basic Research (grant № 21-53-53012) is gratefully acknowledged. The authors would like to thank the Center for X-ray Diffraction Methods and the Interdisciplinary Center for Nanotechnology of Research Park of Saint Petersburg State University.

References

[1] M. Armand, J.M. Tarascon, Building better batteries, Nature 451 (2008) 652–657. https://doi.org/10.1038/451652a.

[2] M. Armand, P. Axmann, D. Bresser, M. Copley, K. Edström, C. Ekberg, D. Guyomard, B. Lestriez, P. Novák, M. Petranikova, W. Porcher, S. Trabesinger, M. Wohlfahrt-Mehrens, H. Zhang, Lithium-ion batteries – Current state of the art and anticipated developments, J. Power Sources 479 (2020) 228708. https://doi.org/10.1016/j.jpowsour.2020.228708.

[3] Y. Shi, Y. Chen, L. Shi, K. Wang, B. Wang, L. Li, Y. Ma, Y. Li, Z. Sun, W. Ali, S. Ding,

An overview and future perspectives of rechargeable zinc batteries, Small 16 (2020) 2000730. https://doi.org/10.1002/smll.202000730.

[4] M. Song, H. Tan, D. Chao, H.J. Fan, Recent advances in Zn-ion batteries, Adv. Funct. Mater. 28 (2018) 1802564. https://doi.org/10.1002/adfm.201802564.

[5] N. Zhang, X. Chen, M. Yu, Z. Niu, F. Cheng, J. Chen, Materials chemistry for rechargeable zinc-ion batteries, Chem. Soc. Rev. 49 (2020) 4203–4219. https://doi.org/10.1039/c9cs00349e.

[6] L.E. Blanc, D. Kundu, L.F. Nazar, Scientific challenges for the implementation of Zn-ion batteries, Joule 4 (2020) 771–799. https://doi.org/10.1016/j.joule.2020.03.002.

[7] X. Zhang, L. Wang, H. Fu, Recent advances in rechargeable Zn-based batteries, J. Power Sources 493 (2021) 229677. https://doi.org/10.1016/j.jpowsour.2021.229677.

[8] N. Liu, B. Li, Z. He, L. Dai, H. Wang, L. Wang, Recent advances and perspectives on vanadium- and manganese-based cathode materials for aqueous zinc ion batteries, J. Energy Chem. 59 (2021) 134–159. https://doi.org/10.1016/j.jechem.2020.10.044.

[9] C. Xu, B. Li, H. Du, F. Kang, Energetic zinc ion chemistry: The rechargeable zinc ion battery, Angew. Chemie - Int. Ed. 51 (2012) 933–935. https://doi.org/10.1002/anie.201106307.

[10] J. Lee, J.B. Ju, W. Il Cho, B.W. Cho, S.H. Oh, Todorokite-type MnO_2 as a zinc-ion intercalating material, Electrochim. Acta 112 (2013) 138–143. https://doi.org/10.1016/j.electacta.2013.08.136.

[11] B. Lee, H.R. Lee, H. Kim, K.Y. Chung, B.W. Cho, S.H. Oh, Elucidating the intercalation mechanism of zinc ions into α-MnO_2 for rechargeable zinc batteries, Chem. Commun. 51 (2015) 9265–9268. https://doi.org/10.1039/c5cc02585k.

[12] M.H. Alfaruqi, J. Gim, S. Kim, J. Song, J. Jo, S. Kim, V. Mathew, J. Kim, Enhanced reversible divalent zinc storage in a structurally stable α-MnO_2 nanorod electrode, J. Power Sources 288 (2015) 320–327. https://doi.org/10.1016/j.jpowsour.2015.04.140.

[13] H. Pan, Y. Shao, P. Yan, Y. Cheng, K.S. Han, Z. Nie, C. Wang, J. Yang, X. Li, P. Bhattacharya, K.T. Mueller, J. Liu, Reversible aqueous zinc/manganese oxide energy storage from conversion reactions, Nat. Energy 1 (2016) 16039. https://doi.org/10.1038/nenergy.2016.39.

[14] X. Guo, J. Zhou, C. Bai, X. Li, G. Fang, S. Liang, Zn/MnO_2 battery chemistry with dissolution-deposition mechanism, Mater. Today Energy 16 (2020) 100396. https://doi.org/10.1016/j.mtener.2020.100396.

[15] S. Islam, M.H. Alfaruqi, V. Mathew, J. Song, S. Kim, S. Kim, J. Jo, J.P. Baboo, D.T. Pham, D.Y. Putro, Y.-K. Sun, J. Kim, Facile synthesis and the exploration of the zinc storage

mechanism of β-MnO_2 nanorods with exposed (101) planes as a novel cathode material for high performance eco-friendly zinc-ion batteries, J. Mater. Chem. A 5 (2017) 23299–23309. https://doi.org/10.1039/C7TA07170A.

[16] W. Liu, X. Zhang, Y. Huang, B. Jiang, Z. Chang, C. Xu, F. Kang, β-MnO_2 with proton conversion mechanism in rechargeable zinc ion battery, J. Energy Chem. 56 (2021) 365–373. https://doi.org/10.1016/j.jechem.2020.07.027.

[17] S. Chou, F. Cheng, J. Chen, Electrodeposition synthesis and electrochemical properties of nanostructured γ-MnO_2 films, J. Power Sources 162 (2006) 727–734. https://doi.org/10.1016/j.jpowsour.2006.06.033.

[18] M.H. Alfaruqi, V. Mathew, J. Gim, S. Kim, J. Song, J.P. Baboo, S.H. Choi, J. Kim, Electrochemically induced structural transformation in a γ-MnO_2 cathode of a high capacity zinc-ion battery system, Chem. Mater. 27 (2015) 3609–3620. https://doi.org/10.1021/cm504717p.

[19] M.H. Alfaruqi, J. Gim, S. Kim, J. Song, D.T. Pham, J. Jo, Z. Xiu, V. Mathew, J. Kim, A layered δ-MnO_2 nanoflake cathode with high zinc-storage capacities for eco-friendly battery applications, Electrochem. Commun. 60 (2015) 121–125. https://doi.org/10.1016/j.elecom.2015.08.019.

[20] C. Qiu, X. Zhu, L. Xue, M. Ni, Y. Zhao, B. Liu, H. Xia, The function of Mn^{2+} additive in aqueous electrolyte for Zn/δ-MnO_2 battery, Electrochim. Acta 351 (2020) 136445. https://doi.org/10.1016/j.electacta.2020.136445.

[21] L. Tang, X. Ji, H. Luo, M. Yao, S. Cheng, Achievement of high durability of δ-MnO_2 based pseudocapacitive electrode enabled by Zn doping induced reattachment, J. Alloys Compd. 834 (2020) 155117. https://doi.org/10.1016/j.jallcom.2020.155117.

[22] B. Lee, C.S. Yoon, H.R. Lee, K.Y. Chung, B.W. Cho, S.H. Oh, Electrochemically-induced reversible transition from the tunneled to layered polymorphs of manganese dioxide, Sci. Rep. 4 (2014) 6066. https://doi.org/10.1038/srep06066.

[23] L. Chen, Q. An, L. Mai, Recent Advances and prospects of cathode materials for rechargeable aqueous zinc-ion batteries, Adv. Mater. Interfaces 6 (2019) 1900387. https://doi.org/10.1002/admi.201900387.

[24] D. Selvakumaran, A. Pan, S. Liang, G. Cao, A review on recent developments and challenges of cathode materials for rechargeable aqueous Zn-ion batteries, J. Mater. Chem. A. 7 (2019) 18209–18236. https://doi.org/10.1039/c9ta05053a.

[25] W. Shi, W.S.V. Lee, J. Xue, Recent development of Mn-based oxides as zinc-ion battery cathode, ChemSusChem 14 (2021) 1634–1658. https://doi.org/10.1002/cssc.202002493.

[26] Y. Yu, J. Xie, H. Zhang, R. Qin, X. Liu, X. Lu, High-voltage rechargeable aqueous zinc-

based batteries: Latest progress and future perspectives, Small Sci. 1 (2021) 2000066. https://doi.org/10.1002/smsc.202000066.

[27] N. Zhang, F. Cheng, J. Liu, L. Wang, X. Long, X. Liu, F. Li, J. Chen, Rechargeable aqueous zinc-manganese dioxide batteries with high energy and power densities, Nat. Commun. 8 (2017) 405. https://doi.org/10.1038/s41467-017-00467-x.

[28] S. Zhao, B. Han, D. Zhang, Q. Huang, L. Xiao, L. Chen, D.G. Ivey, Y. Deng, W. Wei, Unravelling the reaction chemistry and degradation mechanism in aqueous Zn/MnO_2 rechargeable batteries, J. Mater. Chem. A 6 (2018) 5733–5739. https://doi.org/10.1039/c8ta01031e.

[29] W. Sun, F. Wang, S. Hou, C. Yang, X. Fan, Z. Ma, T. Gao, F. Han, R. Hu, M. Zhu, C. Wang, Zn/MnO_2 battery chemistry with H^+ and Zn^{2+} coinsertion, J. Am. Chem. Soc. 139 (2017) 9775–9778. https://doi.org/10.1021/jacs.7b04471.

[30] V. Soundharrajan, B. Sambandam, S. Kim, S. Islam, J. Jo, S. Kim, V. Mathew, Y. K. Sun, J. Kim, The dominant role of Mn^{2+} additive on the electrochemical reaction in $ZnMn_2O_4$ cathode for aqueous zinc-ion batteries, Energy Storage Mater. 28 (2020) 407–417. https://doi.org/10.1016/j.ensm.2019.12.021.

[31] M. Chamoun, W.R. Brant, C.W. Tai, G. Karlsson, D. Noréus, Rechargeability of aqueous sulfate Zn/MnO_2 batteries enhanced by accessible Mn^{2+} ions, Energy Storage Mater. 15 (2018) 351–360. https://doi.org/10.1016/j.ensm.2018.06.019.

[32] G. Fang, C. Zhu, M. Chen, J. Zhou, B. Tang, X. Cao, X. Zheng, A. Pan, S. Liang, Suppressing manganese dissolution in potassium manganate with rich oxygen defects engaged high-energy-density and durable aqueous zinc-ion battery, Adv. Funct. Mater. 29 (2019) 1808375. https://doi.org/10.1002/adfm.201808375.

[33] S. Guo, L. Qin, T. Zhang, M. Zhou, J. Zhou, G. Fang, S. Liang, Fundamentals and perspectives of electrolyte additives for aqueous zinc-ion batteries, Energy Storage Mater. 34 (2021) 545–562. https://doi.org/10.1016/j.ensm.2020.10.019.

[34] H. Chen, S. Cai, Y. Wu, W. Wang, M. Xu, S.J. Bao, Successive electrochemical conversion reaction to understand the performance of aqueous Zn/MnO_2 batteries with Mn^{2+} additive, Mater. Today Energy 20 (2021) 100646. https://doi.org/10.1016/j.mtener.2021.100646.

[35] Y. Zeng, X. Zhang, Y. Meng, M. Yu, J. Yi, Y. Wu, X. Lu, Y. Tong, Achieving ultrahigh energy density and long durability in a flexible rechargeable quasi-solid-state Zn–MnO_2 battery, Adv. Mater. 29 (2017) 1700274. https://doi.org/10.1002/adma.201700274.

[36] L. Liu, Y.C. Wu, L. Huang, K. Liu, B. Duployer, P. Rozier, P.L. Taberna, P. Simon, Alkali ions pre-intercalated layered MnO_2 nanosheet for zinc-ions storage, Adv. Energy Mater. 11 (2021) 26–28. https://doi.org/10.1002/aenm.202101287.

[37] S.H. Kim, S.M. Oh, Degradation mechanism of layered MnO_2 cathodes in $Zn/ZnSO_4/MnO_2$ rechargeable cells, J. Power Sources 72 (1998) 150–158. https://doi.org/10.1016/S0378-7753(97)02703-1.

[38] Y.H. Chu, C.C. Hu, K.H. Chang, Electrochemical quartz crystal microbalance study of amorphous MnO_2 prepared by anodic deposition, Electrochim. Acta 61 (2012) 124–131. https://doi.org/10.1016/j.electacta.2011.11.106.

[39] P.K. Nayak, N. Munichandraiah, An EQCM investigation of capacitance of MnO_2 in electrolytes containing multivalent cations, J. Electroanal. Chem. 685 (2012) 37–40. https://doi.org/10.1016/j.jelechem.2012.09.003.

[40] P.R. Jadhav, M.P. Suryawanshi, D.S. Dalavi, D.S. Patil, E.A. Jo, S.S. Kolekar, A.A. Wali, M.M. Karanjkar, J.H. Kim, P.S. Patil, Design and electro-synthesis of 3-D nanofibers of MnO_2 thin films and their application in high performance supercapacitor, Electrochim. Acta 176 (2015) 523–532. https://doi.org/10.1016/j.electacta.2015.07.002.

[41] D.P. Dubal, D.S. Dhawale, T.P. Gujar, C.D. Lokhande, Effect of different modes of electrodeposition on supercapacitive properties of MnO_2 thin films, Appl. Surf. Sci. 257 (2011) 3378–3382. https://doi.org/10.1016/j.apsusc.2010.11.028.

[42] QCM200 Operation and service manual, Stanford Research Systems, 2004.

[43] B. Lee, H.R. Seo, H.R. Lee, C.S. Yoon, J.H. Kim, K.Y. Chung, B.W. Cho, S.H. Oh, Critical role of pH evolution of electrolyte in the reaction mechanism for rechargeable zinc batteries, ChemSusChem 9 (2016) 2948–2956. https://doi.org/10.1002/cssc.201600702.